TECHNIQUE TO EXTRACT RIGID-BODY DATA FROM SHOCK-INDUCED STRUCTURAL LOADS

F.K. Lu* and M. Gopalan†

University of Texas at Arlington, Arlington, Texas 76019

and

P.L. Walter‡ and W.E. Williamson§

Texas Christian University, Fort Worth, Texas 76129

It is often desired to solely measure the time-varying rigid-body (quasi-static) response of a structural system under transient loading conditions. Due to the transfer functions of the measuring transducers, the measuring systems, and the mechanical structure to which they are affixed, the measured responses can be complex. The goal of this study was to optimize a measurement system to enable the extraction of meaningful rigid-body data. A novel scaling method, based on the 95 percent amplitude attenuation point of the filters, was developed to allow meaningful comparison between different analog filters. The optimal filter was found to be a sixth-order Bessel filter with its 95% amplitude attenuation point placed at 70 percent of the resonant frequency of the structure. The sweet spot for locating the accelerometer and its isolator within the body was also identified.

Nomenclature

a	= acceleration
B	= Butterworth filter
Be	= Bessel filter
c	= damping coefficient
C1	= Chebychev, 0.1 dB, filter
C5	= Chebychev, 0.5 dB, filter
$[D]$	= dynamics matrix
F	= force
k	= stiffness of accelerometer sensing element; also $k = 1,\ldots,N$, element in finite element model
$[K]$	= stiffness matrix
m	= mass of accelerometer sensing element
$[M]$	= mass matrix
$r(\omega)$	$= \omega/\omega_n$, normalized frequency
ω_n	$= \sqrt{k/m}$, natural frequency
ω_d	$= \omega_n\sqrt{1-\zeta^2}$, damped natural frequency
ζ	$= c/\left(2\sqrt{km}\right)$, damping ratio

‡Professor and Director, Aerodynamics Research Center, Box 19018, Arlington, TX 76019. Associate Fellow AIAA

*Graduate Student, Mechanical and Aerospace Engineering Department, Box 19018, Arlington, TX 76019; presently, engineer, RBI-Gearhart, Fort Worth, Texas.

†Senior Lecturer, Department of Engineering, TCU Box 298650

§Professor and Chair, Department of Engineering, TCU Box 298650

Introduction

The ability to extract rigid-body data from shock-induced loads is important in applications such as the measurement of forces in short-duration hypervelocity test facilities,[1] pulse detonation engines,[2] and penetrators for planetary and lunar sample return missions[3–5] and for obvious military applications.[6] Often, the desire is to solely measure the time-varying rigid-body (quasi-static) response of a structural system under shock loading conditions. Due to the transfer functions of the measuring transducers, the measuring systems, and the mechanical structures to which they are affixed, the measured responses can be complex. The goal of this study is to optimize a measurement system to enable the extraction of meaningful rigid-body data. The emphasis of this study is on penetrators although the technique can be employed elsewhere.

The most common measurement in penetrometry is the penetrator's dynamic response. This measurement enables inferences to be made concerning the geomaterial's characteristics. The measurements can also be used to validate structural models predicting penetrator-geomaterial interaction. The ability to make real-time decisions on board enables the control of select functions during penetration. For example, the ability to detect a change in the composition of the geomaterial could be used to trigger the storage of measured data for retrieval or trigger the transmission of data to a remote receiver.

Real-time decisions require the comparison of measured information against a prescribed or predetermined standard. Therefore, the ability to generate accu-

rate and reliable predictions and the ability to obtain high-quality data of sufficient bandwidth for comparison with these predictions is of utmost importance. This paper focuses primarily on the latter, that is, the measurement system design to enable real-time decision-making in penetration events. This includes details on transducer selection, transducer placement, anti-aliasing filter type, anti-aliasing filter frequency selection, signal conditioning amplifier location and the survivability of the signal processing components.

Predictions of the loads imposed on the penetrator during specific events must first be obtained before the quality of the measurement system can be assessed. The output from the modeled penetrator and measurement system can then be compared against the predicted inputs to optimize the system design and to assess errors.

In order to assess the quality of the measurement system, we need to first generate predictions for loads imposed on the penetrator during specific penetration events. These predictions are then input to the combined penetrator structural model and the measurement system. The output is then compared to the predicted inputs to optimize the system design and provide error assessment.

Modeling of penetrator-geomaterial interaction

Modeling of penetration-geomaterial interaction involves theory, empiricism and finite element methods in a custom software program in combination with commercially available software. The rigorous analysis of penetrators and their interaction with targets is often performed using powerful supercomputers.

The first step in modeling penetration events usually involves the use of hydrocodes.[7] Hydrocodes have been developed over the past few decades to simulate dynamic events, especially those that include high shock strengths. Hydrocodes are used to calculate the strains, stresses, forces and accelerations of both the penetrator and the target geomaterial as a function of time and space. These programs include simple details about the penetrator geometry and impact conditions.

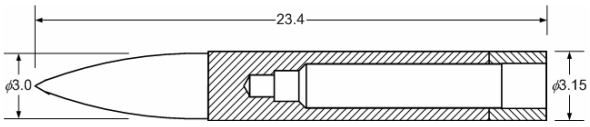

Figure 1. Sketch of penetrator (dimensions in in.).

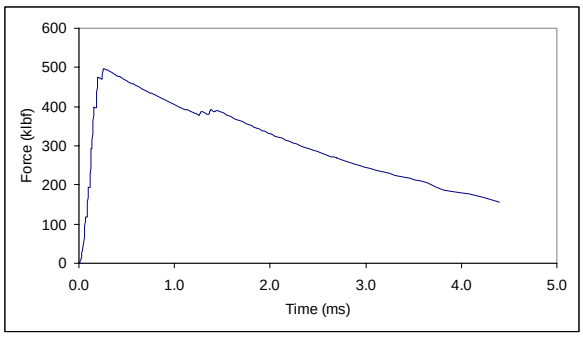

Figure 2. Force–time history of miniature penetrator traversing a layer of hard concrete.

The main limitation of hydrocodes is their computational complexity. Hydrocodes are primarily used to predict the early time (O(10 ms)) behavior of simple geometries and targets. This is useful in providing simple guidelines for payload and penetrator survivability during the initial high-shock impacts.

There also exist theoretical and empirical models that predict the rigid body forces (and therefore rigid body accelerations) that act on the penetrator during penetration events.[8–12] PENCRV3D is one such software program that allows the prediction of penetration events through concrete, soil and air.[13]

A shortcoming of present models is that they attempt to model the low frequency response of the penetrator (by treating them as rigid bodies) but ignores the higher frequency structural characteristics of the penetrator and their effect on the measured data. The problem, simply stated, is that while the predictions provided by present modeling capability are generally those of rigid body response, the data available for real time decision making contains within it higher frequency structural content as well as errors induced by the measurement system. This fact complicates the comparisons between the measured and predicted responses, thereby compromising the ability to make decisions in real time. The best course of action is to acquire data of sufficient quality and bandwidth so that real-time comparisons (between predicted and measured parameters) can be made more effectively.

In order to provide design guidance for these measurement systems, specific test cases where penetration events have been modeled are needed. An example of the predicted axial force time input for a miniature penetrator used for testing purposes (Fig. 1) as it traverses through a single layer of concrete is shown in Fig. 2. This penetrator is approximately 23.4 in. in length and 3 in. in diameter, and weighs approximately 28.8 lbf.

The prediction shows the entry of the both the nose and tail of the penetrator into the layer. The calculation was stopped before the modeled penetrator came to a complete stop. This resulted in a non-zero force value at the end of the data set. PENCRV3D assumes that the penetrator is a rigid body and has infinite stiffness and finite mass. The predicted forces are all along the axial axis of the penetrators and are essentially the rigid body forces acting on these penetrators. These forces can now be used as inputs into a finite element model and the

structural response of the penetrator at various locations can be calculated.

Penetrator Structural Response

Using the rigid body predictions typified by Fig. 2 and the mass of the penetrator, the rigid body accelerations can be easily calculated as

$$a_{rigidbody} = F_{rigidbody} / m_{penetrator} \quad (1)$$

However, the actual acceleration response at any location of the penetrator can vary significantly from rigid body accelerations due to the elastic nature of the penetrator. In order to calculate the structural response of the penetrator, a simple finite element model can be created. Modal superposition is then used to predict the acceleration response of the penetrator at various internal locations due to the imposed input loads. It is assumed that during the penetration event, the penetrator body does not experience stresses and strains beyond the yield limit of the material used. This allows a simple elastic model to be used.

The penetrator shown in Fig. 1 can be represented as five axial cylindrical sections of varying cross sections with an added point mass to represent the tip of the nose. The sketch of the equivalent cylindrical model of the penetrator is shown in Fig. 3. The equivalent cylindrical model can now be used to create a corresponding finite element model. The series of cylinders for the penetrator can be discretized into elements of equal length, and mass and stiffness matrices generated. The elements themselves are modeled as two degree-of-freedom rod elements. The mass and stiffness matrices for a single element can be written as

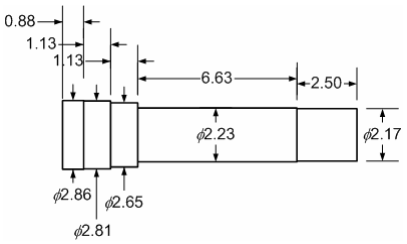

Figure 3. Sketch of cylindrical model (dimensions in in.).

$$m = \frac{\rho A L}{6}\begin{bmatrix} 2 & 1 \\ 1 & 2 \end{bmatrix} \quad (2)$$

$$k = \frac{AE}{L}\begin{bmatrix} 1 & -1 \\ -1 & 1 \end{bmatrix} \quad (3)$$

where A is the cross sectional area of the cylinder at that location, L is the length of element, E is the modulus of elasticity and ρ is the mass density. The principles of linearity and superposition can now be applied to generate the mass and stiffness matrices for these

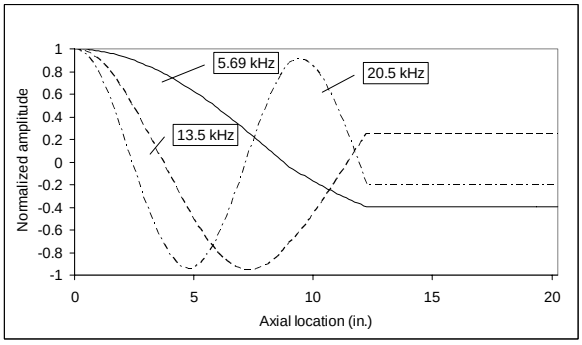

Figure 4. Normalized mode shapes.

penetrators. Assuming $\rho = 9.322 \times 10^{-3}$ slugs/in.^{3}, $E = 30 \times 10^6$ lbf/in^2, and $L = 0.125$ in., we obtain the global mass matrix $[M]$ and the global stiffness matrix $[K]$. In building the mass and stiffness matrices, it is assumed that the boundary conditions on the penetrator are free-free, that is, none of the nodes of the elements used in the finite element model are restrained. This assumption has been used based on the agreement of empirical data gathered from instrumented penetration tests with modal tests performed under free-free conditions. From the global mass and stiffness matrices, we can obtain a dynamics matrix

$$[D] = [M]^{-1}[K] \quad (4)$$

The eigenvalues and eigenvectors for the penetrator can be solved. The zeroth (rigid body), first, second and third eigenvalues are 0, 5.69, 13.55 and 20.6 kHz, respectively. The normalized mode shapes are shown in Fig. 4.

Note that for a model (as exemplified in Fig. 3) with N elements, the number of nodes is $N+1$, which is also equal to the total number of degrees of freedom. The nose is modeled as a point mass at node N. From the matrix of eigenvectors $[\Phi]$ and the vector of input force loads $\{P\}$, the modal mass, modal stiffness and the modal loads can be obtained via

$$[\bar{M}] = [\Phi]^T [M][\Phi] \quad (5)$$

$$[\bar{K}] = [\Phi]^T [K][\Phi] \quad (6)$$

$$\{\bar{P}\} = [\Phi]^T \{P\} \quad (7)$$

In using modal superposition to calculate the structural response of the penetrator, it is assumed that the rigid body forces act on the nose of the penetrator, that is, the rigid body force-time input defined in Fig. 2 acts on node N. Therefore the vector $\{P\}$ can be defined as

$$P[k] = 0 \qquad N > k \geq 0$$
$$P[k] = F(t) \qquad k = N \tag{8}$$

where $F(t)$ is the force input load to the penetrator. The structural response of the penetrator to a generalized input $F(t)$ can now be computed.

The acceleration response $A_k(t)$ of the penetrator at node k due to a generalized input loading $F(t)$ can be found using

$$A_k(t) = \left(\frac{d^2}{dt^2} U_k(t) \right) + \frac{F(t)}{m_{penetrator}} \tag{9}$$

$$U_k(t) = \left(\sum_{r=1}^{3} \Phi_{kr} \eta_r(t) \right) \tag{10}$$

$$\eta_r(t) = \frac{\vec{P}_r}{\vec{K}_{rr}} * S_r(t) \tag{11}$$

where $m_{penetrator}$ is the total mass of the penetrator, $*$ is the convolution operator and

$$S_r(t) = 1 - e^{-\zeta \omega_n t} \left(\cos(\omega_d t) + \frac{\zeta \omega_n}{\omega_d} \sin(\omega_d t) \right) \tag{12}$$

is the step response of a second-order system with the same natural frequency as the mode under question. The value of ζ attributed to the penetrator metal case and any contained material has been assumed to be 0.03 and is representative of the damping found in metals. The structural response at any internal location can be found from an arbitrary input loading applied to the nose using Eqs. (1)–(12).

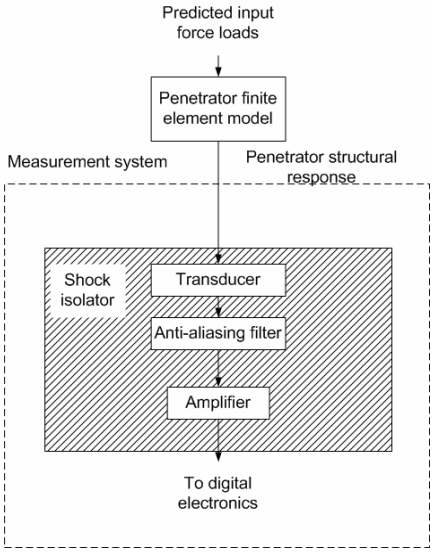

Figure 5. Measurement system block diagram.

Measurement System Overview

The measurement system must be capable of acquiring data of sufficient quality and bandwidth to enable real-time decision making. Figure 5 shows a block diagram of the major analog components of the measurement system, including the transducer, signal conditioning amplifier and the anti-aliasing filter. The digital electronics that follow the analog measurement system, including the analog-to-digital converter, micro-controllers and digital signal processors will not be discussed in this paper. Their design is influenced by the specific control algorithms that are applied. However, optimizing the design of the analog components is a necessity for any measurement system independent of subsequent digital electronics.

In Fig. 5, the predicted input loads by PENCRV3D, say, are used as inputs to the finite element model of the penetrator. The structural response calculated from the finite element model is then used as input into a measurement system model. The output from these responses can in turn be compared to the original predictions to enable optimization of measurement system design.

Since the existing predictive capability is limited to rigid-body response, the measurement system must be capable of extracting the low frequency response of the penetrator while eliminating its higher frequency structural response. This can be done by low-pass filtering of the analog signal. The low-pass filtering also eliminates distortions caused by aliasing. However, low-pass filtering of the analog signal introduces errors in the form of phase shifts, time delays, spreading of the rise time of the signal, and causes amplitude distortion. The type of filter used and the filter cutoff frequency must be carefully selected to minimize these distortions and errors.

Usually, the transducer's signal is first amplified to acceptable levels and then low-pass filtered to eliminate aliasing and extract the needed bandwidth. However, since the structural response can be significantly greater in magnitude than the rigid body response, over-ranging of the amplifier may be possible, resulting in a clipped signal. Low-pass filtering of this clipped signal masks the effect of the clipping. To prevent clipping, the signal can be low-pass filtered prior to amplification.

Transducer Selection and Isolator Design

Transducers considered for use in measurement systems to enable real-time decision-making in penetration events are strain gages and accelerometers. Both are capable of responding to the structural vibration of the penetrator. Several factors favor accelerometers over strain gages for the present application. The signal levels from strain gage circuits are typically in the mV range and are limited by the minimum wall thickness required in the pene-

trator case, that is, the thickness of the penetrator case has to be above a minimum value to ensure structural integrity and thus places an upper bound on the magnitude of strain in the case. This leads directly to low levels of strain, resulting in low signal levels and therefore poor signal-to-noise ratios. Accelerometers, on the other hand, can be tailored to specific ranges and can provide better signal magnitudes (up to hundreds of mV) and therefore better signal to noise ratios.

Another reason for selecting accelerometers over strain gages has to do with measurement of bending modes. Strain gages mounted on the case of the penetrator respond to both bending and axial strains. In order to cancel the contamination of the bending strain on the axial strain measurement, a second strain gage has to be mounted 180 deg around the circumference of the penetrator case. This requires additional wiring and interconnects, increasing the complexity of manufacturing the penetrator and measurement system. Accelerometers respond only to accelerations along their axis of measurement and can be mounted relatively easily along the axis of the penetrator. This results in the direct measurement of axial accelerations without the need for further hardware or wiring. In addition, the ability to measure pure axial accelerations makes the comparison of the measured data to predictions easier and more reliable.

Accelerometer

The accelerator that was chosen is an Endevco (Capistrano, California) model 7270A. This accelerometer is capable of measuring up to and beyond 200,000*g*, and has very high resonant frequencies (1.2 MHz for the 200,000*g* model). This transducer can be modeled as a second-order system with a base acceleration input, a known resonant frequency and a very low damping. The damping is assumed to be $\zeta = 0.003$. This low damping coefficient means that the amplification at resonance is very high. Thus, it is essential that inputs with frequencies at or near the accelerometer's resonance must be prevented from entering the accelerometer as they could damage or destroy the transducer.

Isolator

The interaction of the penetrator and the geomaterial during impact into hard layers such as concrete can be separated into two major periods. The first period is tens or a few hundred ms long and can be referred to as the material response phase. In the period beyond the material response, the structural response of the penetrator dominates, see "Penetrator Structural Response" above.

Immediately after impact, shock waves propagate at through the penetrator and are reflected by internal boundaries and free surfaces, imparting a complex chain of step velocities and acceleration impulses to the accelerometer. The magnitude, duration and occurrence of these events are indeterminate but it is safe to assume that they occur every time the penetrator transitions from a soft geomaterial (air, dirt) to a hard geomaterial (e.g. rocks, concrete). These impulses excite the accelerometer's resonance and cause the accelerometer flexure to oscillate at very high amplitudes. Due to this large amplification, the output from the accelerometer can easily over-range the signal conditioning equipment and the flexure of the accelerometer could be damaged. Thus, it is of utmost importance that the accelerometer be designed to survive during this early time period. This is best accomplished by using a shock isolator.

The primary goal of the shock isolator is to progressively mitigate high frequency inputs to the accelerometer so as to prevent over-ranging and breakage during the material response time period. Ideally, the shock isolator is designed to transmit rigid-body frequencies with flat amplitude and linear phase response, and mitigate all higher frequencies. However, materials that can be used to build shock isolators have high internal losses and are very rate and temperature dependent. Due to these limitations, the best course of action is to design a shock isolator that provides flat frequency response to as high a rigid-body frequency as possible while still providing adequate attenuation to isolate the accelerometer from the impulsive loading. By designing the shock isolator to begin rolling off well above the rigid-body frequencies, the effects of rate and temperature on the rigid-body frequencies can be reduced.

A block diagram of a conceptual shock isolator is shown in Fig. 6. The accelerometer is compressed between two layers of thin isolator gaskets. A spring–mass model of a conceptual shock isolator is shown in Fig. 6. In this figure, the springs represent the stiffness of the isolation material. For our purposes, the damping of the isolator gasket material has been ignored. From this model, the resonant frequency of the accelerometer-shock isolator assembly can be calculated as

$$\omega_{ISO} = \sqrt{2AE/(mt)} \qquad (13)$$

where A is the area of the accelerometer in contact with the isolator gasket, E is the equivalent modulus elasticity of the gasket material, m is the mass of the accelerometer and t is the thickness of the gasket and. It can be noteed that the mass of the accelerometer cabling has been ignored. This implies that the cables should be properly strain relieved in order to prevent unwanted loading on the isolator assembly. From the manufacturer's data, $m = 1.5$ gm and $A = 0.157$ in^2.

For the penetrator example, the second axial resonance occurs at approximately 13 kHz. As we are interested in recovering rigid-body data, this frequency is

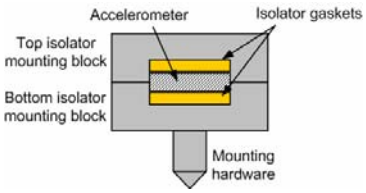

a. Block diagram.

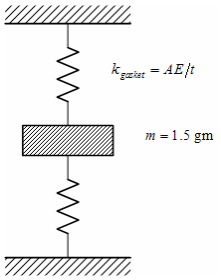

b. Spring–mass model.

Figure 6. Conceptual isolator design.

used as the upper bounding case, that is, the isolator assembly must have flat amplitude and linear phase response to at least 13 kHz. To ensure this, the resonance of the isolator must be at least $\omega_{ISO} = 65$ kHz. With such an isolator, we can assume that the accelerometer will survive the initial material response phase of the penetration process and that the isolator will have no significant effect on the measured data. Thus the effects of the isolator can be ignored and the isolator can be treated as a component with a unity transfer function. Now that a sensor and an isolation strategy have been selected, the next step is to determine the optimal placement of the sensor and isolator assembly.

Transducer Placement

Since the penetrator is a structural system with various resonances and associated mode shapes, the placement of the sensor at different locations will result in different time histories. Let the penetrator's transfer function at node k from an input $F(t)$ at node N be defined as

$$H_k = \frac{\left| fft(U_k(t)) \right|}{\left| fft(F(t)) \right|} \qquad (14)$$

where the operator *fft* is the fast Fourier transform of the time history in question. To calculate the transfer function of the penetrator at various locations along its length, a decaying exponential input of unit peak can be used. This exponential input, as shown in Fig. 7, decays to 10 percent of its initial value in 5 ms. Using Eq. (14), the transfer functions at these locations can be calculated, some of which are shown in Fig. 8.

Figure 8 shows that the transfer function of the penetrator varies along its length. It can therefore be surmised that there is a location along the penetrator length where the response of a transducer would be optimal, in terms of the recovery of rigid-body response. In other words, we are interested in preserving the flat amplitude response to as high a frequency as possible. In an infinitely rigid structure, this flat amplitude response would extend to infinity.

Figure 4 shows that the mode shape for the lowest non-zero mode vanishes at a certain location along the penetrator. A transducer placed at this location will respond to primarily the second and third axial modes and will have a transfer function whose amplitude response is flat to higher frequencies. This is the optimal location for transdcer placement as it maximizes the flat amplitude response and thus allows the best possible reproduction of the rigid body data. For the present example, the "sweet spot" is 8.75 in. from the tail. In the finite element model, with 99 nodes, this location is node 70. The transfer function at this node is shown in Fig. 9.

Analog Filter Selection

The extraction of rigid-body data from the structural dynamics requires the use of a low-pass filter. Such a filter inevitably introduces time delay and signal distortion. Therefore, its selection cannot be arbitrary and care must be given to the choice of filter type, filter pole order and the placement of the filter's cut-off frequency.

There are three major filter types in regular use in analog signal processing, namely, Butterworth, Bessel and Chebyshev filters. The Butterworth filter is designed to have the maximal flat amplitude response, the Bessel filter is designed to maximize phase linearity and the Chebyshev filter excels in its transition from pass-band to stop-band. Of these three, the Chebyshev filter allows ripple in the pass-band. Two common pass-band ripple values are 0.5 and 0.1 dB. In this study, four filter types—Butterworth, Bessel, Chebyshev 0.5d B and Chebyshev 0.1 dB—of second, fourth, sixth and eighth order are examined.

Figure 10 shows the responses of second-order filters. The amplitude for all of these filters roll off at 12 dB/octave. Note that each filter has its unique frequency response. To facilitate inter-comparison between the curves, the filters have been normalized to have the same 95% attenuation point at $r(\omega) = 1$. The characteristics of the other filter types are not shown for brevity.

Moreover, each of the filters has a unique step response. In order to compare these varying step responses, all the filters have been arbitrarily scaled to provide 95% attenuation at 10 rad/s. The value of 10 rad/s has no physical significance except to allow the inter-comparison of the step responses. Figure 11 shows the step responses of second-order filters. The step

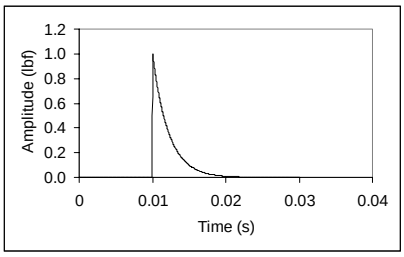

Figure 7. Unit exponential input.

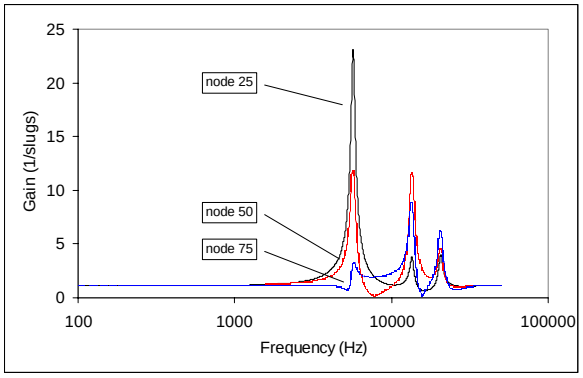

Figure 8. Transfer functions at nodes 25, 50 and 75.

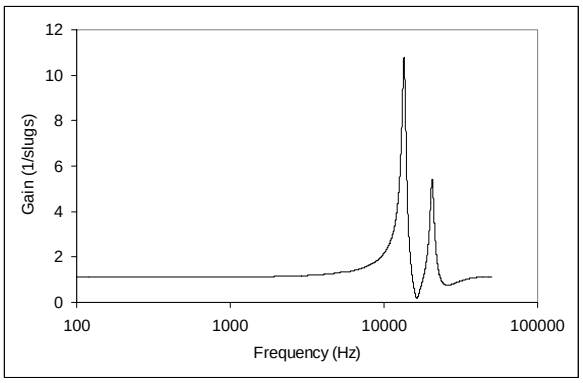

Figure 9. Transfer functions at sweet spot (node 70).

responses of other filters are not shown for brevity, although it should be stated that other than the Bessel filter, the others show damped oscillatory behavior.

It is apparent from Figs. 10 and 11 that a filter's spectral characteristics and rise time are important. The rise time of the filter conditioning the output from the accelerometer controls the time it takes to identify transitions in the geomaterial during the penetrator's traverse. Thus, the rise time of the filter must be minimized so as to enable the fastest detection of layer transitions in the geomaterial. The second concerns the settling time of the filter. The settling time controls the time required before a void in the geomaterial can be accurately detected. Minimizing the settling time allows for fast detection of voids. The third concerns the time delay of the

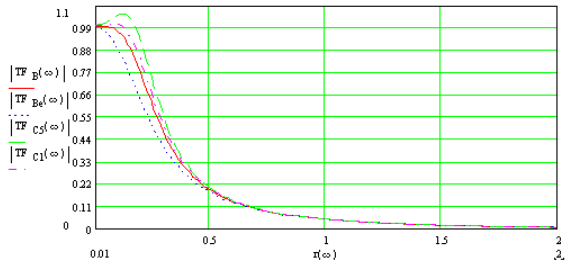

a. Amplitude spectra.

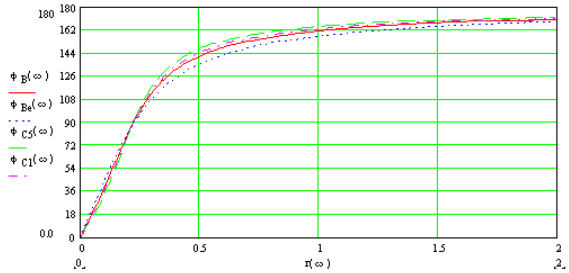

b. Frequency spectra.

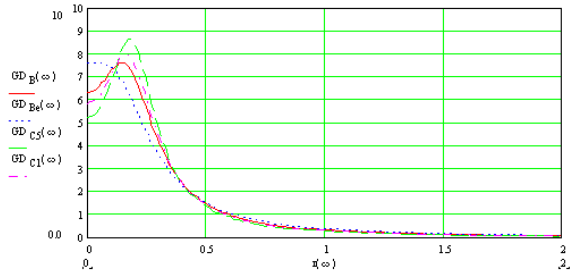

c. Group-delay spectra.

Figure 10. Response of second-order filters.

filter. The filter creates a time delay in the process of making real-time decisions based on the filtered data. As with rise time and settling-time, the time delay of the

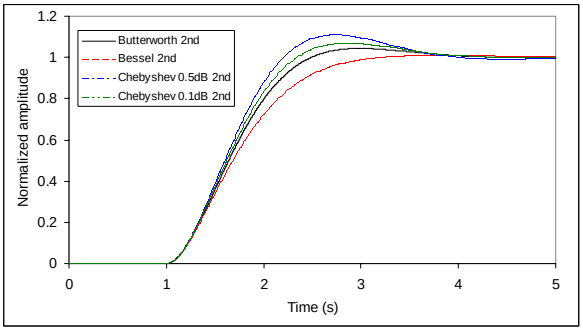

Figure 11. Step response of second-order filters.

filter must be minimized. However, these three criteria are not mutually exclusive and therefore the goal is to pick a filter type and order that will provide the best possible compromise between these three requirements.

Table 1 shows the rise and settling times of various filters. Rise time, as defined here, is the 10 to 90 percent value of the step response. The filters were assigned values from 1 to 16 corresponding to fastest to slowest rise times. Table 1 also shows the two percent settling of these filters with a similar grading scheme. Finally, an overall figure of merit is assigned based on the average of the scores for the rise and settling times, as also displayed in Table 1. The results indicate that the 8th-order Butterworth and the 6th-order Bessel filters are the best. These two filters will be investigated further to select the better of the two.

Filter Cutoff Frequency and Amplifier Placement

After identifying the optimal filters, we now need to determine the optimal cutoff frequencies. A parametric study on the optimal filter cutoff frequency requires first that a representative structural system with arbitrary resonant frequency be modeled. Any structural system can be modeled through its first resonance as a second-order system with appropriate damping. In this study, the representative system was modeled with a resonant frequency of 10 rad/sec and a damping coefficient of 0.03. This result is shown in the curve labeled '2nd' in Fig. 12. The amplitude-frequency curves of the two candidate filters selected above can be combined with that of the structural system to create a set of composite transfer function curves. The composite transfer functions thus created are also shown in Fig. 12. The figure shows that the composite amplitude-frequency curves differ significantly between filter types and filter placement.

So far, the two filters selected were based on their rise and settling time performances. The results can be further enhanced by exploiting the compensating effect of the filters and filter cutoff placement. This is done by performing a step response analysis on the composite system. This evaluation encompasses the structural response of the penetrator, the response of the accelerometer (assumed to be unity at low frequencies), the response of the shock isolator (also assumed to be unity at low frequencies) and the responses of the two filter types. The results are displayed for the 6th-order Bessel filter in Table 2 and for the 8th-order Butterworth filter in Table 3. The data show that the peak error increases as the filter's 95 percent attenuation frequency is increased.

Table 1. Filter effectiveness.

	Order	Rise Time (s)	Score	Settling Time (s)	Score	Average Score
Butterworth	2	0.960	15	2.664	10	12.5
Butterworth	4	0.514	9	2.087	5	7.0
Butterworth	6	0.441	7	2.330	6	6.5
Butterworth	8	0.420	5	2.343	7	6.0
Bessel	2	1.206	16	1.917	4	10.0
Bessel	4	0.680	12	1.198	2	7.0
Bessel	6	0.595	11	1.191	1	6.0
Bessel	8	0.575	10	1.278	3	6.5
Chebyshev 0.5 dB	2	0.813	13	2.658	9	11.0
Chebyshev 0.5 dB	4	0.432	6	2.856	12	9.0
Chebyshev 0.5 dB	6	0.391	2	3.653	14	8.0
Chebyshev 0.5 dB	8	0.391	1	3.656	15	8.0
Chebyshev 0.1 dB	2	0.891	14	2.695	11	12.5
Chebyshev 0.1 dB	4	0.457	8	2.430	8	8.0
Chebyshev 0.1 dB	6	0.403	4	2.951	13	8.5
Chebyshev 0.1 dB	8	0.397	3	3.669	16	9.5

Moreover, the peak delay decreases as the filter's 95 percent attenuation frequency increases. The settling time (either 2 or 5 percent) of the composite system to a step input reaches a minimum value as the filter's 95 percent attenuation frequency increases, and then begins to increase again. This is because at low frequencies, the transient response of the filter dominates the settling time while at high frequencies the resonance of the structure begins to dominate. Note that although the results shown in Table 2 are for a representative system with a resonance of 10 rad/s, the results generalize to any frequency.

From the data in Tables 2 and 3, it can be seen that the composite response using the 6th-order Bessel filter outperforms that using the 8th-order Butterworth filter for decreasing peak error, reducing peak delay and reducing settling time. In addition, the best compromise while optimizing all the parameters appears to be the 6th-order Bessel filter with its 95 percent attenuation point set at 70 percent of the lowest resonant frequency of interest in the penetrator. The second best choice is the 8th-order Butterworth filter with its 95 percent attenuation point set at 80 percent of the lowest resonant frequency of interest.

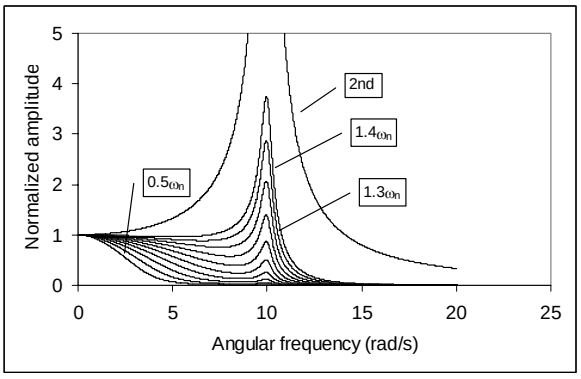

a. Sixth-order Bessel filter.

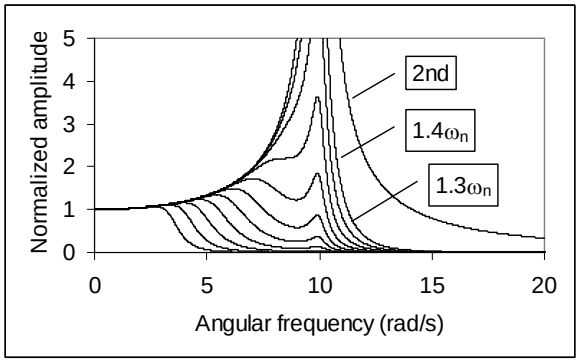

b. Eighth-order Butterworth filter.

Figure 12. Composite amplitude-frequency plot.

Table 2. Response of 6th-order Bessel filter applied to composite system.

	Peak Error (%)	Peak Delay (sec)	2% Settling Time (sec)	5% Settling Time (sec)
$0.5\omega_n$	0.78	2.37	2.01	1.90
$0.6\omega_n$	1.30	2.02	1.66	1.56
$0.7\omega_n$	1.41	1.56	1.38	1.33
$0.8\omega_n$	3.11	1.45	1.53	1.18
$0.9\omega_n$	4.07	1.42	3.39	0.94
$1.0\omega_n$	6.31	1.40	5.23	2.26
$1.1\omega_n$	14.43	0.85	6.60	3.58
$1.2\omega_n$	24.35	0.80	7.67	4.66
$1.3\omega_n$	34.22	0.76	8.73	5.72
$1.4\omega_n$	43.80	0.73	8.99	6.52

Table 3. Response of 8th-order Butterworth filter applied to composite system

	Peak Error (%)	Peak Delay (sec)	2% Settling Time (sec)	5% Settling Time (sec)
$0.5\omega_n$	20.12	2.14	4.77	3.25
$0.6\omega_n$	22.11	1.77	4.01	2.72
$0.7\omega_n$	24.37	1.52	3.37	2.78
$0.8\omega_n$	28.09	1.33	3.44	2.44
$0.9\omega_n$	36.27	1.15	3.90	2.60
$1.0\omega_n$	47.61	1.05	5.75	2.80
$1.1\omega_n$	60.7	0.99	7.12	4.63
$1.2\omega_n$	73.7	0.91	9.25	6.76
$1.3\omega_n$	86.3	0.86	11.35	8.34
$1.4\omega_n$	99.6	0.82	12.42	9.94

System Response to Modeled Inputs

The previous sections have provided the approach for optimizing the analog filter. This filter is now verified. To do so, the modeled input shown in Fig. 2 is used as the force input to the finite element model of the penetrator. The results are shown in Fig. 13.

Recall that the small peak at approximately 0.0012 s in the data (Fig. 2) is caused by the entry of the tail flare into the target geomaterial. The modeled accelerometer structural response is calculated assuming the measurement transducer is at the 'sweet spot' of the penetrator, which is 8.875 in. from the tail. When placed at this location, the accelerometer does not respond to the first axial mode at 5693 Hz. The filtered data results from the use of the 6th-order Bessel filter set to have its 95 percent attenuation point at 70 percent of the second axial mode at 13549 Hz. Note the good agreement of the magnitude of the pulse peaks between the rigid body input and the filtered response. In addition, the time de-

lay between the filtered data and the modeled input data is seen to be approximately 0.0002 s.

Conclusions

An optimal analog measurement system to enable real-time decision making in penetrators has been developed. Present modeling capability is restricted to predicting rigid body loads acting on penetrators. Highly transient loading such as initial concrete impact and impacts with reinforcing materials are not predicted. As the process of making real-time decisions involves comparing predicted or known amplitudes or response characteristics to measured values, the only meaningful comparison that can be made is between the predicted rigid-body loading and the measured rigid-body acceleration of the penetrator during its traverse. Therefore, it is critical that the best quality rigid-body data be recovered from the structural response of the penetrator while minimizing any distortions introduced by the measurement system.

The recovery of rigid-body data can be accomplished over a region of flat frequency response. Due to the elastic nature of the penetrator, its flat amplitude response extends to frequencies below its lowest resonance. However, the response of an accelerometer varies depending on its mounting location on the penetrator. An optimal location for the placement of the measurement accelerometer was identified, namely, at the penetrator's first axial mode (sweet-spot).

A novel scaling method, based on the 95 percent amplitude attenuation point of the filters, was developed to allow meaningful comparison between common filter types and orders. The step response of these various filters was graded using a relative scale. Two candidate filters (6th-order Bessel and 8th-order Butterworth) were then combined with a representative model of a second-order system to investigate the frequency compensation effects of filter cutoff frequency placement. Based on the step responses of these composite systems, a 6th-order Bessel filter whose 95 percent attenuation point is set at 70 percent of the second axial resonance of the penetrator was determined to be optimal. The efficacy of such an arrangement was demonstrated.

References

[1] Smith, A.L. and D.J. Mee, D.J., "Drag Measurements in a Hypervelocity Expansion Tube, *Shock Waves*, Vol. 6, No. 3, 1996, pp. 161–166.

[2] Cooper, M., Jackson, S., Austin, J., Wintenberger, E. and Shepherd, J.E., "Direct Experimental Impulse Measurements for Detonations and Deflagrations," AIAA 2001–3812, 2001.

[3] Lorenz, R.D. and Shandera, S.E., "Target Effects During Penetrator Emplacement: Heating, TriboElectric Charging, and Mechanical Disruption," *Planetary and Space Science*, Vol. 50, 2002, pp. 163–179.

[4] Surkov, Y.A., Moskaleva, L.P., Shcheglov, O.P., Sheretov, E.P. Kremnev, R.S., Pichkhadze, K.M., Akulov, Y.P. and Dolgopolov, V.P., "Lander and Scientific Equipment for Exploring of Volatiles on the Moon," *Planetary and Space Science*, Vol. 47, 1999, pp. 1051–1060.

[5] Kömle, N.I., Kargl, G. and Ball, A.J., "Determination of Physical Properties of Planetary Sub-Surface Layers by Artificial Impacts and Penetrometry," *Advances in Space Research*, Vol. 28, No. 10, 2001, pp. 1539–1549.

[6] Li, Q.M., Weng, H.J. and Chen, X.W., "A Modified Model for the Penetration into Moderately Thick Plates by a Rigid, Sharp-Nosed Projectile," *International Journal of Impact Engineering*, Vol. 30, No. 2, 2004, pp. 193–204.

[7] Anderson, C.E., Jr., "An Overview of the Theory of Hydrocodes," *International Journal of Impact Engineering*, Vol. 5, 1987, pp. 809–822.

[8] Backman, M.E., and Goldsmith, W., "The Mechanics of Penetration of Projectiles into Targets," *International Journal of Engineering Science*, Vol. 16, 1978, pp. 1–99.

[9] Forrestal, M.J., Altman, B.S., Cargile, J.D. and Hanchak, S.J., "An Empirical Equation for Penetration Depth of Ogive-Nose Projectiles into Concrete Targets. *International Journal of Impact Engineering*, Vol. 15, 1994, pp. 395–405.

[10] Forrestal, M.J. and Luk, V.K., 'Penetration into Soil Targets, *International Journal of Impact Engineering*, Vol. 12, No. 3, 1992, pp. 427–444.

[11] Forrestal, M.J., Tzou, D.Y., Askari, E. And Longcope, B.D., "Penetration into Ductile Metal Targets with Rigid Spherical-Nose Rods," *International Journal of Impact Engineering*, Vol. 16, No. 5/6, 1995, pp. 699–710.

[12] Walker, J.D., Hypervelocity penetration modeling. *International Journal of Impact Engineering*, Vol. 26, 2001, pp. 809–822.

[13] Adley, M.D., Berger, R.P., Cargile, J.D. and White, H.G., "Three-Dimensional Projectile Penetration into Curvilinear Geological/Structure Targets: User's Guide for PENCRV3D v. 2.0. U.S. Army Corp of Engineers Report SL-99-1, Vicksburg, Mississippi, 1999.

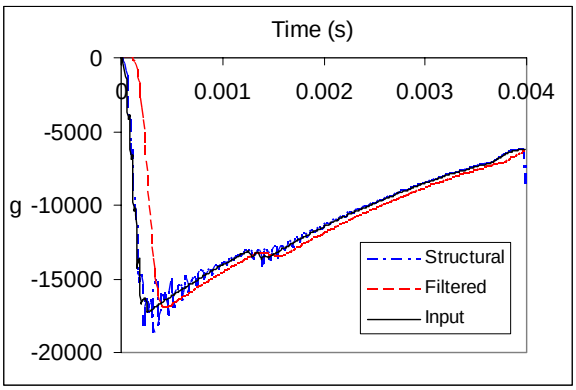

Figure 13. Responses to force input of Fig. 2.